Nonlinear functional relation covering near- and far-marginal stability in ion temperature gradient driven turbulence

OPEN ACCESS
IOP Publishing
Plasma Physics and Controlled Fusion
Plasma Phys. Control. Fusion **64** (2022) 075007 (10pp)
https://doi.org/10.1088/1361-6587/ac6ffc

Nonlinear functional relation covering near- and far-marginal stability in ion temperature gradient driven turbulence

Nakayama T[1,*], M Nakata[1,2,3], M Honda[4], M Nunami[2,5] and S Matsuoka[1,2]

[1] The Graduate University for Advanced Studies, Toki, Gifu 509-5292, Japan
[2] National Institute for Fusion Science, Toki, Gifu 509-5292, Japan
[3] PRESTO, Japan Science and Technology Agency, 418, Honcho, Kawaguchishi, Saitama 332-0012, Japan
[4] Graduate School of Engineering, Kyoto University, Kyoto, Kyoto 615-8530, Japan
[5] Nagoya University, Graduate School of Science, Nagoya, Aichi 464-8603, Japan

E-mail: nakayama.tomonari@nifs.ac.jp

Received 28 February 2022, revised 20 April 2022
Accepted for publication 16 May 2022
Published 6 June 2022

Abstract

A novel nonlinear functional relation of turbulence potential intensity, zonal flow potential intensity, and ion thermal diffusivity that accurately reproduces nonlinear gyrokinetic simulations of toroidal ion temperature gradient (ITG) driven turbulence is proposed. Applying mathematical optimization techniques to find extremal solutions in high-dimensional parameter space, the optimal regression parameters in the functional form are determined to be valid for both near- and far-marginal regime of the ITG stability including the Dimits-shift. Then, the regression error of $\sim$5% is accomplished. In addition, it is clarified that the intensity ratio of the zonal flow and turbulence potential intensity is a crucial factor to determine the reproduction accuracy.

Keywords: plasma turbulence, zonal flow, reduced model, gyrokinetic simulation

(Some figures may appear in colour only in the online journal)

1. Introduction

In order to realize high-performance burning plasmas expected in ITER and DEMO, it is indispensable to elucidate and predict global turbulent transport and profile formations. To this end, the first-principle-based nonlinear gyrokinetic simulation is one of powerful approaches, and many efforts have been devoted to the extensions to global, electromagnetic, and multiple-species treatments (see e.g. [1, 2]). Although much physical information is contained, a huge amount of numerical costs is necessary to carry out the global gyrokinetic simulations over the confinement time, and systematic numerical scans for various operation scenarios are still infeasible.

As a practical approach, various integrated simulations, such as TASK/TASK3D [3–5], TOPICS [6, 7], and GOTRESS+ [8–10], have also been developed. Utilizing simplified/reduced models constructed from theoretical, experimental, and numerical studies, the magnetic equilibria, heating, fueling, neoclassical and turbulent transport, and time evolution of macroscopic radial profiles are individually calculated. The turbulent transport, which often exceeds the neoclassical levels, is of particular importance for the accuracy of predictions by integrated simulations. Construction of a more accurate, but still simplified model that reproduces results of the nonlinear gyrokinetic simulations or the experimental observations is a central issue in tokamak and stellarator turbulence studies.

* Author to whom any correspondence should be addressed.

Theoretical and numerical studies on the simplified models for the turbulent transport have extensively been conducted so far, where some remarkable models such as GLF23 [11], TGLF [12–14], and QuaLiKiz [15] have been proposed in the framework of quasi-linear gyrokinetic and gyrofluid approaches. The effects of multi-scale fluctuations [16] and mean $\boldsymbol{E}\times\boldsymbol{B}$ flow shear [17] are also incorporated. Moreover, a combined modeling based on the linear and nonlinear gyrokinetic simulations has also been explored, where the impacts of turbulence nonlinearity and zonal flow generation on the ion temperature gradient (ITG) driven turbulent thermal transport for ions have been taken into account [18]. An extension to the electron-thermal and particle transport has been applied in the similar manner [19–22].

Furthermore, modeling studies with deep neural networks have actively been addressed as another recent approach [9, 10, 23, 24]. Experimentally and/or numerically produced massive datasets regarding the radial kinetic profiles and the transport fluxes, etc are utilized for the training of multi-layered neural networks. Then, one can rapidly estimate the turbulent transport fluxes or the related diffusivities from the several inputs of known physical parameters such as the safety factor, local background density and temperature, and their logarithmic gradients. Indeed, a semi-empirical neural network model, which was constructed by using the local gyrokinetic simulation and JT-60U experiment data, well reproduces the particle and thermal transport fluxes in neutral-beam-heated plasmas [25, 26]. Although such deep-neural-network-based modelings are powerful, one should note that the physical explainability or interpretability and the extrapolation capability are generally limited in the approach with deep neural networks.

In this study, to construct a more accurate and physically interpretable model, a nonlinear functional relation (NFR) is proposed. The nonlinearity among turbulence, zonal flows, and thermal transport flux in tokamak ITG driven turbulence is phenomenologically incorporated to the NFR by means of the nonlinear gyrokinetic simulations and mathematical optimization techniques. To be applicable to the global turbulent transport with significant variations of the profile gradients [27], our NFR is verified to be valid for a wide range of the physical parameters and the radial domains, including near- and far-marginal ITG stability. Indeed, the importance of the zonal flow effects near the regime of so-called Dimits-shift [28] has been revealed in several gyrokinetic simulation studies regarding the near-marginal or sub-critical turbulence dynamics [29, 30] and the isotope effects [31, 32]. Encompassing such strong zonal flow effects is necessary to accurately predict the dynamical evolutions of the kinetic profiles and the magnetic equilibria. Once the systematic methodology to proposed an accurate NFR is established, various simplified transport models can be induced by combining the conventional modelings [18–22] with linear calculations as in [18]. Also, the phenomenological arguments in the present NFR approach enable us to extract the physical interpretations and useful suggestions to improve the accuracy.

The rest of this paper is organized as follows. In section 2, the gyrokinetic model and the nonlinear simulation results for the tokamak ITG driven turbulence including the Dimits-shift regime are presented. Then, based on three types of NFRs, the identification of their regression parameters by using mathematical optimization techniques is discussed in section 3. Further investigations for a key factor to determine the reproduction accuracy are shown in section 4. The verifications of the accuracy and the versatility are given in section 5. Finally, the paper is summarized in section 6.

2. Toroidal ITG driven turbulence simulation

Gyrokinetic turbulence simulation model and numerical results are summarized in this section. Various datasets regarding the turbulence potential intensity, the zonal flow potential intensity, and the turbulent transport coefficient, which strongly depend on the temperature gradient, are prepared to construct the NFR in sections 3 and 4.

The ITG driven turbulent transport simulations in a tokamak equilibrium are performed by using a gyrokinetic Vlasov simulation code GKV [33]. Since the nonlinear modeling incorporating the strong zonal flow effects is of particular focus in this study, the electrostatic limit with the adiabatic electron response is assumed for simplicity. The gyrokinetic-Poisson equations in Fourier wavenumber representation are summarized as follows:

$$\left[\frac{\partial}{\partial t}+v_{\parallel}\nabla_{\parallel}+i\omega_{\mathrm{Ds}}-\left(\frac{e_{\mathrm{s}}\mu}{m_{\mathrm{i}}}\nabla_{\parallel}B\right)\frac{\partial}{\partial v_{\parallel}}\right]\delta f_{\mathrm{s}\boldsymbol{k}_{\perp}} - \frac{1}{B}\sum_{\boldsymbol{k}'_{\perp}+\boldsymbol{k}''_{\perp}=\boldsymbol{k}_{\perp}}\boldsymbol{b}\cdot(\boldsymbol{k}'_{\perp}\times\boldsymbol{k}''_{\perp})J_0(k'_{\perp}\rho_{\mathrm{s}})\delta\phi_{\boldsymbol{k}'_{\perp}}\delta f_{\mathrm{s}\boldsymbol{k}''_{\perp}} = \frac{e_{\mathrm{s}}F_{\mathrm{Ms}}}{T_{\mathrm{s}}}(i\omega_{*T\mathrm{s}}+i\omega_{\mathrm{Ds}}-v_{\parallel}\nabla_{\parallel})J_0(k_{\perp}\rho_{\mathrm{s}})\delta\phi_{\boldsymbol{k}_{\perp}}+C_{\mathrm{s}}, \quad (1)$$

$$\left[k_{\perp}^2+\frac{1}{\varepsilon_0}\sum_{\mathrm{s}}\frac{e_{\mathrm{s}}^2 n_{\mathrm{s}}}{T_{\mathrm{s}}}(1-\Gamma_{0\mathrm{s}\boldsymbol{k}_{\perp}})\right]\delta\phi_{\boldsymbol{k}_{\perp}} = \frac{1}{\varepsilon_0}\sum_{\mathrm{s}}e_{\mathrm{s}}\int d\boldsymbol{v}\,J_0(k_{\perp}\rho_{\mathrm{s}})\delta f_{\mathrm{s}\boldsymbol{k}_{\perp}}, \quad (2)$$

where $\delta f_{\mathrm{s}\boldsymbol{k}_{\perp}}=\delta f_{\mathrm{s}\boldsymbol{k}_{\perp}}(z,v_{\parallel},\mu,t)$ denotes the perturbed gyrocenter distribution function for the particle species 's', which is represented in the fluxtube coordinates (see [34, 35] for more details). Here, $\boldsymbol{k}_{\perp}=(k_x,k_y)$, $\boldsymbol{b}$, B, $\delta\phi_{\boldsymbol{k}_{\perp}}$, μ, e_{s}, m_{s}, and T_{s} are the perpendicular wavenumber vector, the unit vector parallel to the field line, the magnetic field strength, the electrostatic potential fluctuation, the magnetic moment, the electric charge, the particle mass, and the temperature for each particle species, respectively. The drift frequency, the diamagnetic frequency, and the gyroradius are denoted by ω_{Ds}, $\omega_{*T\mathrm{s}}$, and ρ_{s}, respectively. The finite gyroradius effects are represented by the zeroth-order Bessel function J_0 and $\Gamma_0=e^{-b}I_0(b)$ with $b=(k_{\perp}\rho_{\mathrm{ti}})^2$, where the zeroth-order modified Bessel function, the ion thermal speed, and the ion thermal gyroradius are I_0, $v_{\mathrm{ti}}=\sqrt{T_{\mathrm{i}}/m_{\mathrm{i}}}$, and $\rho_{\mathrm{ti}}=m_{\mathrm{i}}v_{\mathrm{ti}}/e_{\mathrm{i}}B$, respectively. Maxwellian distribution and the collision operator are represented by F_{M} and C_{s}, respectively.

The turbulent thermal transport flux in the radial direction Q_r is given by

$$Q_r = \mathrm{Re}\left\langle \sum_{\boldsymbol{k}_\perp} \int d\boldsymbol{v} \left(\frac{m_\mathrm{s} v^2}{2} - T_\mathrm{s}\right) \delta f_{\mathrm{s}\boldsymbol{k}_\perp} \delta \boldsymbol{v}^*_{\boldsymbol{E}\boldsymbol{k}_\perp} \cdot \nabla r \right\rangle$$
$$= \left\langle \sum_{\boldsymbol{k}_\perp} \int d\boldsymbol{v} \left(\frac{m_\mathrm{s} v^2}{2} - T_\mathrm{s}\right) \frac{\boldsymbol{b} \times \boldsymbol{k}_\perp \cdot \nabla r}{B} \times \mathrm{Im}\left[\frac{\delta f_{\mathrm{s}\boldsymbol{k}_\perp}}{\delta \phi_{\boldsymbol{k}_\perp}}\right] |\delta \phi_{\boldsymbol{k}_\perp}|^2 \right\rangle. \quad (3)$$

Here, $\delta \boldsymbol{v}_{\boldsymbol{E}\boldsymbol{k}_\perp} = i\boldsymbol{b} \times \boldsymbol{k}_\perp \delta \phi_{\boldsymbol{k}_\perp}/B$ denotes the $\boldsymbol{E} \times \boldsymbol{B}$ drift velocity driven by the electrostatic potential fluctuations. The superscript '$*$' means the complex conjugate. The flux surface average is denoted by $\langle \cdots \rangle$. One finds that the turbulent flux is proportional to the product of the fluctuation amplitude $|\delta \phi_{\boldsymbol{k}_\perp}|^2$ and the phase-difference of $\mathrm{Im}[\delta f_{\mathrm{s}\boldsymbol{k}_\perp}/\delta \phi_{\boldsymbol{k}_\perp}]$ as shown in the second equality of equation (3). The turbulent diffusivity is defined by $\chi_\mathrm{s} = -Q_r/(n_\mathrm{s}\, \partial T_\mathrm{s}/\partial r)$, where n_s, r, R, and $1/L_T \equiv -(\partial \ln T_\mathrm{s}/\partial r)$ mean the background density, the radial position, major axis, and the logarithmic temperature gradient, respectively.

Spatially averaged turbulence potential intensity $\mathcal{T}$ and zonal flow potential intensity $\mathcal{Z}$ are defined as follows:

$$\mathcal{T} \equiv \frac{1}{2} \sum_{k_x, k_y \neq 0} \langle |\delta \phi_{k_x, k_y}|^2 \rangle, \quad (4)$$

$$\mathcal{Z} \equiv \frac{1}{2} \sum_{k_x} \langle |\delta \phi_{k_x, k_y = 0}|^2 \rangle. \quad (5)$$

In order to propose the NFR among $\mathcal{T}$, $\mathcal{Z}$, and χ_i, R/L_T-dependence of each quantity is investigated. The heat flux Q_r is generally given by the second order correlation of $\delta \phi_{\boldsymbol{k}_\perp}$ and $\delta f_{\mathrm{s}\boldsymbol{k}_\perp}$, which is determined by the nonlinear gyrokinetic equation in equation (1). On the other hand, when the nonlinearity in equation (1) is neglected, the turbulent flux in equation (3) is reduced to so-called quasi-linear flux Q_r^QL as follows:

$$Q_r^\mathrm{QL} = \mathrm{Re}\left\langle \sum_{\boldsymbol{k}_\perp} \mathcal{L}_{\boldsymbol{k}_\perp} |\delta \phi_{\boldsymbol{k}_\perp}|^2 \right\rangle,$$
$$\mathcal{L}_{\boldsymbol{k}_\perp} = \int d\boldsymbol{v}\, i \frac{e_\mathrm{s} F_\mathrm{Ms} k_y}{T_\mathrm{s} B} \left(\frac{m v^2}{2}\right) \frac{\omega_{*T\mathrm{s}} + \omega_\mathrm{Ds} - k_\parallel v_\parallel}{\omega_{\boldsymbol{k}_\perp} - \omega_\mathrm{Ds} - k_\parallel v_\parallel}. \quad (6)$$

Here, $\omega_{\boldsymbol{k}_\perp} = \omega_r + i\gamma$ denotes the complex frequency that is composed of the mode frequency as the real part and the growth rate as the imaginary part. Through the relation of $|\delta \phi_{\boldsymbol{k}_\perp}|^2 \sim \mathcal{T}$, Q_r^QL can be approximated to $Q_r^\mathrm{QL} \sim C\mathcal{T}^\delta$, where C is a constant and $\delta = 1$.

Table 1 summarizes the physical parameters used in the simulation. The linear and nonlinear simulations were performed for a wide range of the ITG R/L_T at two normalized radial positions $\rho \equiv r/a$ in a tokamak magnetic configuration, where a is the minor radius of the plasma. The safety factor and the magnetic shear are denoted by q and $\hat{s}$. The logarithmic density gradient R/L_n is fixed to 2.2. The phase-space grid points of $(n_{k_x}, n_{k_y}, n_z, n_{v_\parallel}, n_\mu) = (129, 20, 64, 48, 12)$ are used, where $\mu \equiv m_\mathrm{s} v_\perp^2/2B$. $k_{x(\mathrm{min})}\rho_\mathrm{ti} = 0.0251$(at $\rho = 0.5$), 0.108(at $\rho = 0.75$), $k_{y(\mathrm{min})}\rho_\mathrm{ti} = 0.075$, and the velocity domain of $0 \leqslant v_\perp \leqslant 4v_\mathrm{ti}$, and $-4v_\mathrm{ti} \leqslant v_\parallel \leqslant 4v_\mathrm{ti}$ are considered. In total, 17 nonlinear ITG turbulence simulations for weakly collisional plasmas were performed. Figure 1 shows the time evolution of the turbulent heat diffusivity in the gyro-Bohm unit $\chi_\mathrm{i}/\chi_\mathrm{i}^\mathrm{GB}$, where $\chi_\mathrm{i}^\mathrm{GB} \equiv \rho_\mathrm{ti}^2 \nu_\mathrm{ti}/R$. Note that the time in the horizontal axis is normalized by the maximum ITG-mode growth rate γ_max. The statistical steady states for $t\gamma_\mathrm{max} \geqslant 50$ are confirmed for all cases. In this paper, the time window of $(100 \leqslant t\gamma_\mathrm{max} < 300)$ is considered for the average of $\bar{\chi}_\mathrm{i}/\chi_\mathrm{i}^\mathrm{GB}$, $\bar{\mathcal{T}}$, and $\bar{\mathcal{Z}}$. The overline is the time-averaging symbol, which is, hereafter, omitted for simplicity.

Figure 2(a) shows the R/L_T-dependence of $\chi_\mathrm{i}/\chi_\mathrm{i}^\mathrm{GB}$ and the maximum ITG-mode growth rate γ_max. One can see a slight difference between the critical gradient of the ITG instability and the effective gradient driving the thermal transport near $R/L_T \sim 4$, which is so-called the Dimits-shift [28]. Here, the critical gradient for the ITG instability is estimated by zero value of the fitting function of data for $R/L_T = 4 \sim 5$, $R/L_T = 4 \sim 5$, and the width of the Dimits-shift is evaluated as $\Delta(R/L_T) = R/L_T|_{\text{finite } \chi_\mathrm{i}/\chi_\mathrm{i}^\mathrm{GB}} - R/L_T|_{\text{ITG crit. } \gamma_\mathrm{max}} = 0.861$ at $\rho = 0.5$ and $\Delta(R/L_T) = 0.296$ at $\rho = 0.75$. The ratio of the zonal flow potential intensity to the total fluctuations $\mathcal{Z}/(\mathcal{T} + \mathcal{Z})$ as a function of R/L_T is shown in figure 2(b). One

Table 1. Value and range of each parameter used in the simulations.

Parameter	Value and range
Radial position ρ	0.5 and 0.75
Safety factor q	1.41 and 2.34
Magnetic shear $\hat{s}$	0.88 and 1.84
Ion temperature gradient R/L_T	4–12
Density gradient R/L_n	2.2
Collisionality ν_{ii}^*	0.056

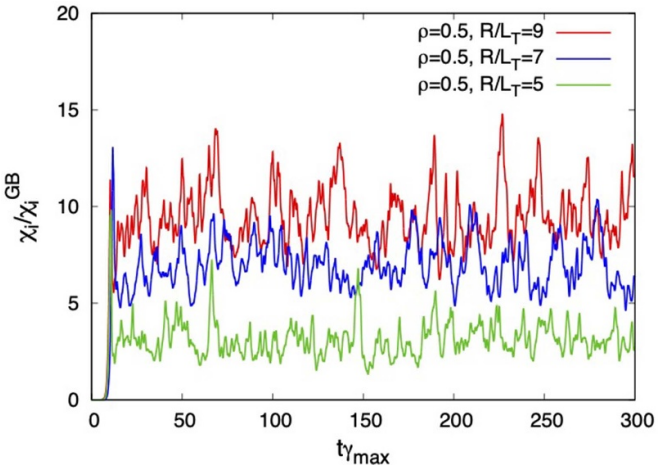

Figure 1. Time evolutions of turbulent diffusivity $\chi_\mathrm{i}/\chi_\mathrm{i}^\mathrm{GB}$ at $\rho = 0.5$. Each curve corresponds to the cases for $R/L_T = 5, 7, 9$, respectively.

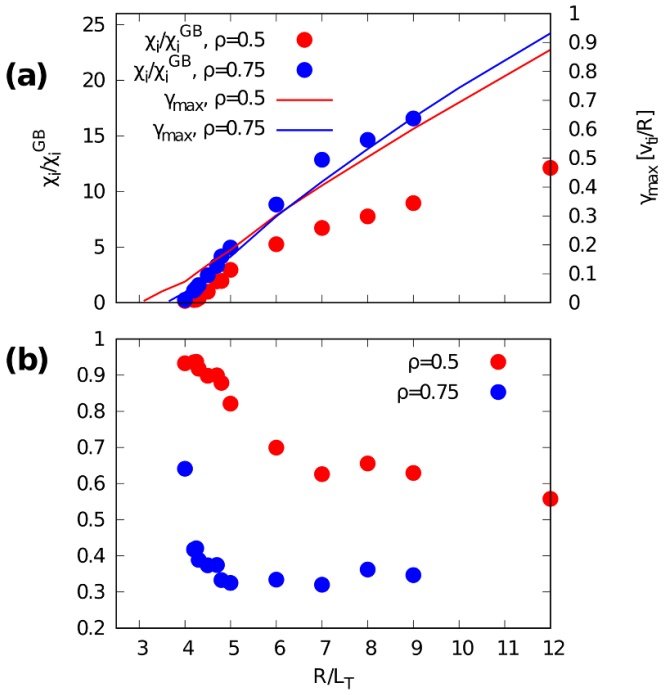

Figure 2. (a)Temperature gradient dependence of χ_i/χ_i^{GB} evaluated by nonlinear simulations (symbols) and γ_{max} $[v_{ti}/R]$ by linear analysis (lines). (b) The ratio of the zonal flow potential intensity $\mathcal{Z}$ to the total fluctuation amplitude $(\mathcal{T}+\mathcal{Z})$.

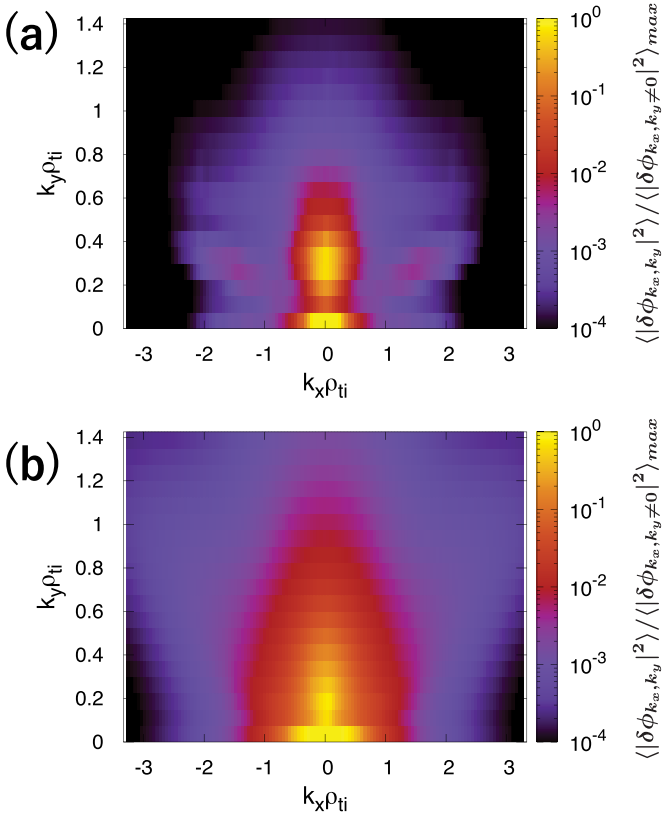

Figure 3. Wavenumber spectra of turbulence potential fluctuations for (a) $\rho=0.5, R/L_T=4.5$, and (b) $\rho=0.5, R/L_T=9$.

finds a significantly larger zonal flow ratio $\mathcal{Z}/(\mathcal{T}+\mathcal{Z})$ near the critical gradient, where the transport reduction occurs. For the lager temperature gradient region of $R/L_T \geqslant 6$, the zonal flow ratio indicates a moderate dependence. The magnitude of Dimits-shift discussed here indicates a positive correlation not only to the relative intensity $\mathcal{Z}/(\mathcal{T}+\mathcal{Z})$, but also to the residual zonal flow level [36–38]. From the linear zonal flow response, the residual zonal flow levels $\mathcal{K}$ are evaluated as $\mathcal{K}=0.0428(\rho=0.5)$, and $\mathcal{K}=0.0259(\rho=0.75)$, where the analytic estimations in the limit of the large-aspect-ratio circular cross section by Rosenbluth and Hinton [36] are $\mathcal{K}_{RH}=0.145(\rho=0.5)$, and $\mathcal{K}_{RH}=0.0558(\rho=0.75)$. These quantities can be useful to explain the qualitative trends in the nonlinear simulation results in figure 2. Furthermore, the shape of the turbulence potential fluctuation spectrum is exemplified in figure 3. It can be seen that for the turbulence (non-zonal $k_y\neq 0$) and zonal flow ($k_y=0$) components the shape of the spectrum is rather different between the cases with high and low temperature gradients. Such various nonlinear dependence on R/L_T appearing in $\mathcal{T}$, $\mathcal{Z}$, and χ_i is crucial for constructing the simplified transport model, which is valid for a wide parameter range of R/L_T.

3. Nonlinear functional relation

NFRs among $\mathcal{T}$, $\mathcal{Z}$, and χ_i, which accurately reproduce the nonlinear gyrokinetic simulation results, are discussed in this section. Three types of the functional forms F^{QL}, F^{NFR1}, and F^{NFR2} are examined.

First, we consider a functional form F^{QL} that is similar to the quasi-linear approximation (cf equation (6)). F^{QL} is a simple regression to express the turbulent thermal diffusivity χ_i/χ_i^{GB} only by $\mathcal{T}$, which is defined as

$$\frac{\chi_i}{\chi_i^{GB}} \sim F^{QL}(\mathcal{T}) = C_1\mathcal{T}^{\alpha}, \tag{7}$$

where C_1 and α denote the regression parameters to be determined. To determine the regression parameters, figure 4 shows the relationship between $\mathcal{T}$ and χ_i/χ_i^{GB}. As is obviously seen in figure 4, there is the refractive behavior at $\chi_i/\chi_i^{GB}\sim 2.5$, which changes the exponent α significantly. Indeed, when the simulation data is classified as the near- and far-marginal cases with the boundary of $\chi_i/\chi_i^{GB}\sim 2.5$, two exponents are evaluated as $\alpha=0.943$ and $\alpha=0.608$ for the near- and far-marginal cases, respectively [shown by the two straight lines in green (near-marginal) and purple (far-marginal) in the figure 4]. It is, therefore, hard to reproduce χ_i/χ_i^{GB} for a wide parameter range including near- and far-marginal ITG stability by the functional form of equation (7) with only turbulence potential intensity $\mathcal{T}$. Indeed, as will be discussed later in table 2, relatively larger regression error is found for F^{QL} with $C_1=0.208$ and $\alpha=0.733$.

On the other hand, the strong correlation between $\mathcal{Z}/(\mathcal{T}+\mathcal{Z})$ and χ_i/χ_i^{GB} is shown in figures 2(a) and (b) motivate us to consider another type of the functional form, which is applicable for both near- and far-marginal cases.

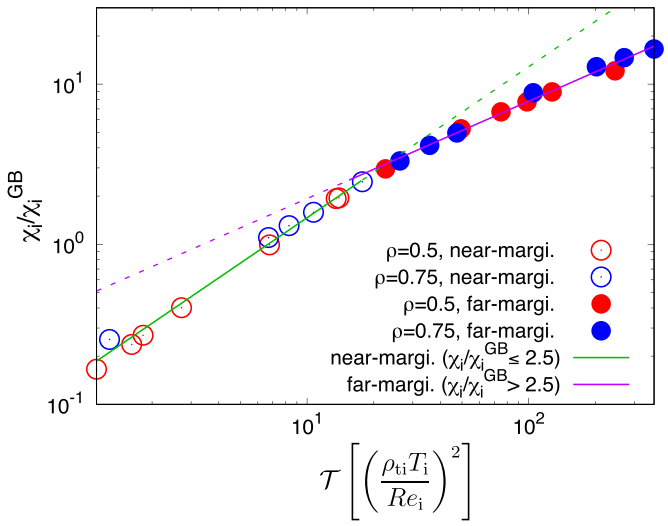

Figure 4. Relation of turbulence potential intensity $\mathcal{T}$ and the turbulent diffusivity $\chi_\mathrm{i}/\chi_\mathrm{i}^\mathrm{GB}$ calculated by GKV.

Here, two nonlinear functional forms of F^NFR1 and F^NFR2 are defined as follows:

$$\frac{\chi_\mathrm{i}}{\chi_\mathrm{i}^\mathrm{GB}} \sim F^\mathrm{NFR1}(\mathcal{T},\mathcal{Z}) = \frac{C_1\mathcal{T}^\alpha}{1+C_2(\mathcal{Z}^\beta/\mathcal{T})}, \tag{8}$$

$$\frac{\chi_\mathrm{i}}{\chi_\mathrm{i}^\mathrm{GB}} \sim F^\mathrm{NFR2}(\mathcal{T},\mathcal{Z}) = \frac{C_1\mathcal{T}^\alpha}{1+C_2(\mathcal{Z}/\mathcal{T})^\beta}, \tag{9}$$

where the zonal flow potential intensity is explicitly incorporated. Note that these kinds of functional forms are not unique, but still satisfy the fundamental phenomenological requirements of

$$\begin{aligned} F^{\mathrm{NFR1,2}}(\mathcal{T},\mathcal{Z}) &\geqslant 0,\\ \lim_{\mathcal{T}\to 0} F^{\mathrm{NFR1,2}}(\mathcal{T},\mathcal{Z}) &= 0,\\ \lim_{\mathcal{T}\to \infty} F^{\mathrm{NFR1,2}}(\mathcal{T},\mathcal{Z}) &= F^\mathrm{QL}(\mathcal{T}),\\ \lim_{\mathcal{Z}\to 0} F^{\mathrm{NFR1,2}}(\mathcal{T},\mathcal{Z}) &= F^\mathrm{QL}(\mathcal{T}),\\ \lim_{\mathcal{Z}\to \infty} F^{\mathrm{NFR1,2}}(\mathcal{T},\mathcal{Z}) &= 0. \end{aligned} \tag{10}$$

Here $(C_1, C_2, \alpha, \beta)$ in equations (8) and (9) are the regression parameters to be determined such that reproduce the nonlinear gyrokinetic simulation data. F^NFR1 is inspired by our previous research [18] corresponding to the model for the far-marginal parameter regime. In this study, a more generalized form is considered, where the exponent of the second term of the denominator is changed from the fixed value of $1/2$ used in [18] to a variable β. A slightly modified form of F^NFR2 is also considered to investigate the impact of intensity ratio of $\mathcal{Z}$ to $\mathcal{T}$ in the denominator. For both functional forms, the second term in the denominator plays role in describing the transport suppression effect by the zonal flows, where the importance of the relative zonal flow intensity in near-marginal cases has been demonstrated in section 2.

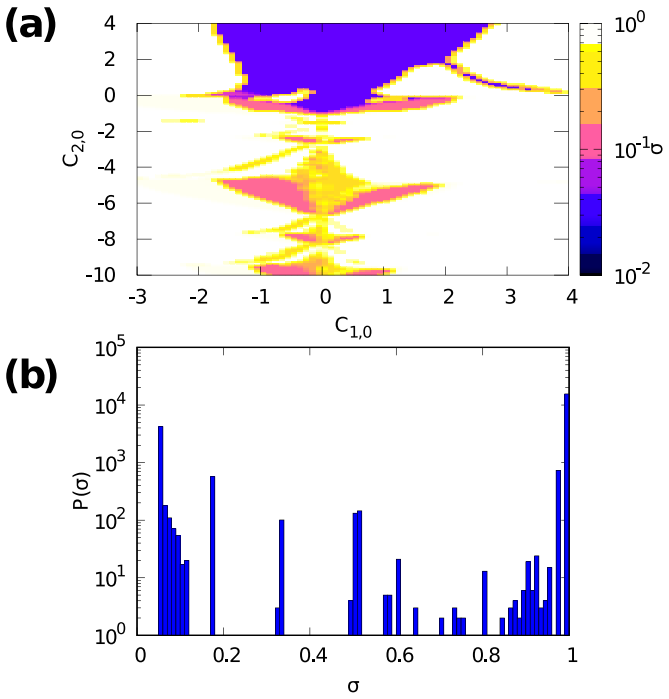

Figure 5. (a) Visualization of the existence of multiple local minima at $(C_{1,0}, C_{2,0})$ with $\alpha_0 = \beta_0 = 0$ fixed. The variations of color correspond to each local minimum. (b) Histogram of σ for the $(C_{1,0}, C_{2,0})$ surface.

The regression error σ to evaluate the reproduction capability is defined by the arithmetic average of the root-mean-square deviations as follows:

$$\sigma = \sqrt{\frac{1}{n}\sum_{j=1}^{n}\left(\frac{F(\mathcal{T}_j,\mathcal{Z}_j)}{\chi_{\mathrm{i},j}/\chi_\mathrm{i}^\mathrm{GB}}-1\right)^2}, \tag{11}$$

where F means the functional relation shown in equations (7)–(9) with no explicit labels. The total data number and the data index are expressed by n and j, respectively. The identification of the NFR to minimize σ is equivalent to the problem of finding the optimal regression parameters $(C_1, C_2, \alpha, \beta)$. An extremal value of σ is given by the solution of a non-convex mathematical optimization problem. Here, the solution corresponds to optimal parameter in F^NFR1 and F^NFR2.

Since the regression error $\sigma = \sigma(C_1, C_2, \alpha, \beta)$, which is the objective function in the context of mathematical optimization, is a nonlinear multi-modal function in the four-dimensional parameter space, a lot of local minima exists in general. Then, depending on the choice of the initial condition, gradient-descent-based searching algorithms often lead to the trapping by a single local minimum. Figure 5(a) shows the example of the initial-value scan with respect to C_1 and C_2, where the contour indicates the different converged values of σ. The existence of several local minima is also emphasized by the histogram $P(\sigma)$ shown in figure 5(b), indicating a multi-modal distribution. Note that the initial values for β and α are fixed to $\beta_0 = 0$ and $\alpha_0 = 0$ in this visualization, where the subscript '0' denotes the initial value.

Table 2. Optimal regression parameters and the regression errors.

Parameter	F^{QL}	F^{NFR1}	F^{NFR2}
C_1	0.208	0.485	0.264
C_2	—	1.30	0.0142
α	0.733	0.611	0.732
β	—	0.243	1.37
σ	0.178	0.0569	0.133

In order to search the high-dimensional solution space as broadly as possible, systematic scans of the initial values should be carried out. However, the discretized grid scan for $(C_{1,0}, C_{2,0}, \alpha_0, \beta_0)$ requires huge computational costs even for the four-dimensional cases. Thus, we introduce a technique to scan a broader parameter range while reducing computational costs. Here, 6 possible combinations of the two-dimensional initial value spaces of $(C_{1,0}, \alpha_0)$,$(C_{1,0}, \beta_0)$, $(C_{1,0}, C_{2,0})$, $(C_{2,0}, \alpha_0)$, $(C_{2,0}, \beta_0)$, and (α_0, β_0), which are chosen from the original parameters, are numerically scanned. The other two initial values are fixed as $(C_{1,0}, C_{2,0}, \alpha_0, \beta_0) = (1, 1, 0, 0)$. The numerical scan of each initial value set is performed in the condition of 200×200 meshes for $-1 \leqslant \alpha_0 \leqslant 1$, $-1 \leqslant \beta_0 \leqslant 1$, $-10 \leqslant C_{1,0} \leqslant 10$, and $-10 \leqslant C_{2,0} \leqslant 10$. Then, the best optimal solution $(C_1, C_2, \alpha, \beta)$ and σ are selected from six results of the two-dimensional scan.

The mathematical optimization algorithm is similar to Levenberg–Marquardt method [39, 40] which combines gradient descent method and Gauss–Newton method. Although the Hessian matrix is approximated by using the Jacobian matrix in Levenberg–Marquardt method, our algorithm directly calculates the Hessian matrix to hold the fast convergence near the local minimum. Then, the Newton method is used when the Hessian matrix is positive definite. Otherwise, the steepest descent method is applied. Typically, 1.4×10^9 steps are needed for one calculation.

The optimal solution $(C_1, C_2, \alpha, \beta)$ and σ for three nonlinear functional forms F^{QL}, F^{NFR1}, and F^{NFR2} are summarized in table 2. One finds the smallest regression error of 0.0569 for F^{NFR1}. As shown in figures 6(a) and (b), the reproduction accuracy of $\chi_{\mathrm{i}}/\chi_{\mathrm{i}}^{\mathrm{GB}}$ is examined, where the estimation by NFR is compared to the nonlinear gyrokinetic simulation results shown in the horizontal axis. The deviation from $\chi_{\mathrm{i}}/\chi_{\mathrm{i}}^{\mathrm{GKV}} = 1$ in the vertical axis indicates the magnitude of local errors. It is clarified from the comparison between F^{QL} and $F^{\mathrm{NFR1,2}}$ that the explicit inclusion of zonal flow potential intensity is crucial for improving the reproduction accuracy of NFR. In addition, we found that the intensity ratio of $\mathcal{Z}$ to $\mathcal{T}$ in the denominator of NFR has a large impact on the regression error. It is emphasized that σ for F^{NFR1} is more than 2.79 times smaller than that in the previous work [$\sigma = 0.159$ [18], 0.12 [19], 0.15 [20], 0.30 [22]], and is valid for wider parameter range including the near- and far-marginal ITG stability.

4. Impacts of zonal flow effects

As is shown in table 2, the regression error of F^{NFR1} is rather smaller than that of F^{NFR2}, where the magnitude of the zonal flow potential intensity $\mathcal{Z}$ in the denominator is slightly different. In this section, the impact of the intensity ratio of $\mathcal{Z}$ to $\mathcal{T}$ on the regression accuracy is examined in more detail to find the reason why F^{NFR1} is more accurate, which enables one to find further optimal parameters. To this end, we define F^{NFR3} as follows:

$$\frac{\chi_{\mathrm{i}}}{\chi_{\mathrm{i}}^{\mathrm{GB}}} \sim F^{\mathrm{NFR3}} = \frac{C_1 \mathcal{T}^{\alpha}}{1 + C_2 (\mathcal{Z}^{\xi}/\mathcal{T})^{\beta}}. \tag{12}$$

The additional parameter ξ is introduced. Using ξ, F^{NFR1} and F^{NFR2} are reproduced by setting $\xi = 0.243$ with $\beta = 1$ and $\xi = 1$ with $\beta = 1.37$, respectively.

Figure 7 shows the regression error of F^{NFR3} as a function of ξ, where σ and the other 4 parameters $(C_1, C_2, \alpha, \beta)$ for given ξ are determined by the same manner in section 3. One finds a nonlinear ξ-dependence of the regression error in the domain of $0 < \xi \leqslant 1$. Even though the regression error for F^{NFR1} is enough small compared to that for F^{NFR2}, a slightly more optimal solution at $\xi = 0.2$ is identified, where $\sigma = 0.0527$.

As can be seen in equation (12), the parameter ξ characterizes the intensity ratio of $\mathcal{Z}$ to $\mathcal{T}$. It is clear from figure 7 that the intensity ratio has a significant impact on σ. This suggests the importance of considering the appropriate intensity ratio of $\mathcal{Z}$ and $\mathcal{T}$. Here, an additional parameter ξ is introduced to characterize the impact of the zonal flow compared to the turbulence intensity. Then, the parameter dependence of $\Lambda \equiv \mathcal{Z}^{\xi}/\mathcal{T}$ in high accuracy and low accuracy is compared. This consideration can clarify the non-negligible

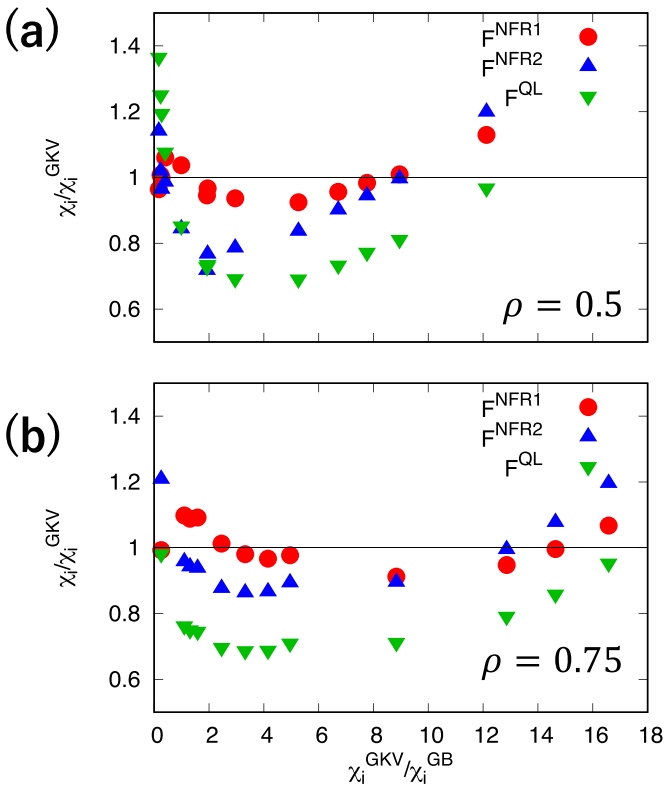

Figure 6. Comparison between NFR (shown bi χ_{i}) and the gyrokinetic simulation results at (a) $\rho = 0.5$ and (b) $\rho = 0.75$. The deviation from $\chi_{\mathrm{i}}/\chi_{\mathrm{i}}^{\mathrm{GKV}} = 1$ indicates the local error.

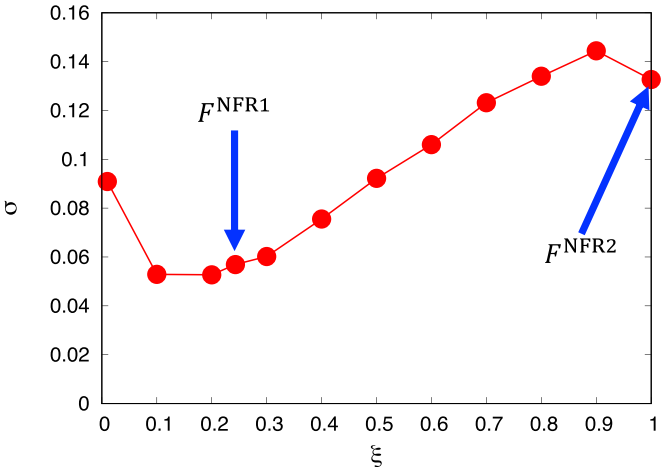

Figure 7. Dependence of the regression error for F^{NFR3} on ξ, where the cases with $\xi = 0.243$ and $\xi = 1$ correspond to F^{NFR1} and F^{NFR2}, respectively.

physics that improves the accuracy of the NFR. To compare, we choose $\xi = \{0.1, 0.2, 0.243\}$ and $\xi = \{0.8, 0.9, 1\}$ as the representative subsets for high and low reproduction accuracy, respectively.

Figures 8(a) and (b) show Λ for the two subsets as a function of the temperature gradient R/L_T. It is demonstrated that the strongly decaying characteristic appears for the subset of $\xi = \{0.1, 0.2, 0.243\}$ with small σ, while nearly flat behavior is observed for the subset of $\xi = \{0.8, 0.9, 1\}$ with larger σ. Then, we can discuss more clearly the different behavior of Λ for the various ξ, by assuming $\Lambda \propto (R/L_T)^{-\eta}$. The fitting exponent η is evaluated as ~ 4.5 for high accuracy cases in figure 8(a), and as ~ 1.5 for low accuracy cases in figure 8(b). The tendency in the former cases with the small regression error is qualitatively consistent with the nonlinear simulation results shown in figure 2(b), where the intensity of relative zonal flow becomes significant in the near-marginal regime with the Dimits-shift. On the other hand, for the latter cases with larger errors, the nearly flat R/L_T-dependence of Λ implies that these NFRs are effectively equivalent to the quasi-linear form of equation (7). Indeed, the regression errors for $\xi = \{0.8, 0.9, 1\}$ are similar to that for F^{QL}, where $C_1 \sim 0.2$, $\alpha \sim 0.7$, and $C_2 \sim 0$. From these observations, it is, thus, crucial for constructing accurate NFR to capture steep behaviors in Λ around the critical gradient.

5. Verification of regression accuracy

In the previous section, the most optimal NFR was identified. The functional form is same as equation (12) where $(C_1, C_2, \alpha, \beta, \xi) = (0.602, 2.01, 0.571, 0.898, 0.2)$ and the regression error $\sigma = 0.0527$. By using the nonlinear simulation data for $\rho = 0.25$, 0.5 , and 0.75, the verification of reproduction accuracy is carried out to examine the versatility of radial direction and temperature gradient. Here, the data for $\rho = 0.25$ is not included in the regression for NFR.

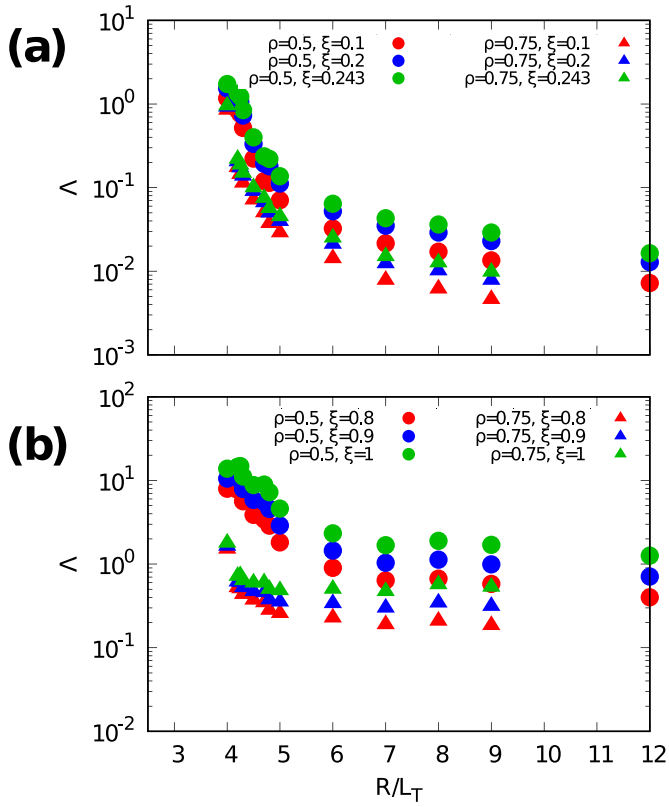

Figure 8. R/L_T-dependence of the intensity ratio $\Lambda = \mathcal{Z}^{\xi}/\mathcal{T}$ in the subsets of (a) $\xi = \{0.1, 0.2, 0.243\}$ in high accuracy and (b) $\xi = \{0.8, 0.9, 1\}$ in low accuracy.

Figure 9 shows the turbulent thermal diffusivity as a function of the temperature gradient R/L_T, where the estimations by NFR are compared with the gyrokinetic simulation results. It is found that our NFR well reproduces the simulation results for $\rho = 0.25$ with the prediction error of $\sigma = 0.0658$, as well as the cases for $\rho = 0.5$ and $\rho = 0.75$. In addition, to verify the accuracy in near-marginal region, the Dimits-shift widths in the NFR and GK-simulation are compared. The Dimits-shift widths of NFR evaluated by the difference between the NFR and the linear calculations are $\Delta(R/L_T) = 0.868$ at $\rho = 0.5$, $\Delta(R/L_T) = 0.294$ at $\rho = 0.75$, and $\Delta(R/L_T) = 0.888$ at $\rho = 0.25$. This is results well reproduces the simulation results $\Delta(R/L_T) = 0.861$ (at $\rho = 0.5$), 0.296 (at $\rho = 0.75$), and 0.9 (at $\rho = 0.25$), respectively. From these results, the accuracy and versatility of the NFR covering near- and far-marginal ITG stability for the several radial positions are demonstrated.

To verify the applicability of NFR in slightly more collisional cases [27], the collisionality ν^* is changed under the conditions of $\rho = 0.5$ and $R/L_T = 4.5$, where $\nu^* = 0.0824, 0.109, 0.162$. Figure 10(a) shows the heat diffusivity and the relative zonal flow intensity for each collisionality. As collisionality increases, the heat diffusivity increases while and the relative zonal flow intensity decreases. Figure 10(b) shows the results of applying the NFR to obtained data. It is demonstrated that the accuracy of the present NFR gradually decreases toward the collisional regime, but still keeps a

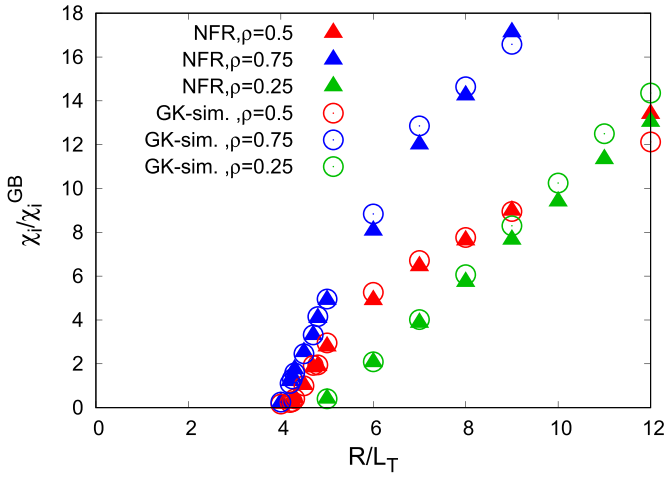

Figure 9. Comparison between NFR and the gyrokinetic simulation results for $\chi_{\rm i}$ at three different radius positions, where the data for $\rho = 0.25$ is not used in the regression.

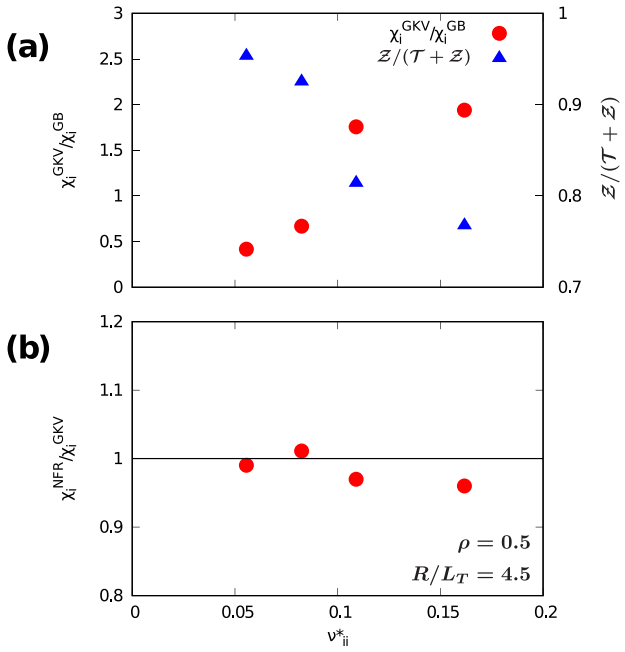

Figure 10. (a) Collisionality dependence of the heat diffusivity $\chi_{\rm i}^{\rm GKV}/\chi_{\rm i}^{\rm GB}$ and the relative zonal flow intensity $\mathcal{Z}/(\mathcal{T}+\mathcal{Z})$. (b) The regression error of applying the NFR to obtained data. The deviation from $\chi_{\rm i}^{\rm NFR}/\chi_{\rm i}^{\rm GKV} = 1$ indicates the local error.

reasonable reproductivity. Such an insensitive feature is associated with the NFR approach with the statistically averaged quantities $\mathcal{T}$ and $\mathcal{Z}$ in which the various parameter dependencies like the collisionality and configuration parameters do not appear explicitly in the NFR.

6. Summary

The aim of this study is to propose a NFR, which is useful for constructing a simplified model for the turbulent transport. To this end, nonlinear gyrokinetic simulations were performed for the tokamak ITG driven turbulence to obtain the parameters used in the construction of the NFR. Here, the electron response was assumed to be adiabatic. The nonlinear dependence of the logarithmic ITG R/L_T on the turbulent thermal diffusivity $\chi_{\rm i}/\chi_{\rm i}^{\rm GB}$, turbulence potential intensity $\mathcal{T}$, and zonal flow potential intensity $\mathcal{Z}$, including the Dimits-shift, were evaluated for the several radial positions.

In order to propose the most plausible NFR that accurately reproduces the gyrokinetic simulations results, several types of the functional form were considered, where $\chi_{\rm i}/\chi_{\rm i}^{\rm GB}$ is expressed as a nonlinear function of $\mathcal{T}$ and $\mathcal{Z}$. The functional form is not unique but still satisfies phenomenological requirements in the ITG driven turbulence.

Applying mathematical optimization techniques to find extremal solutions in high-dimensional parameter space, the optimal regression parameters $(C_1, C_2, \alpha, \beta)$ in the NFR are determined. Then, the regression error of $\sigma = 0.0527$, which is much smaller than that in earlier work [18–22] and in the quasi-linear form $F^{\rm QL}$, is accomplished. Moreover, the present NFR is found to be valid for both near- and far-marginal regimes of the ITG stability, including the Dimits-shift.

It is also clarified that the intensity ratio of the zonal flows and turbulence, $\mathcal{Z}^{\xi}/\mathcal{T}$ with the additional parameter ξ, is a crucial factor to determine the reproduction accuracy. Through the verification using the simulation data for $\rho = 0.25$, which is not applied to the regression, the accuracy and versatility of the NFR covering near- and far-marginal ITG stability for the several radial positions are demonstrated.

The NFR approach contributes to extract the essential turbulent suppression process by the zonal flow in the plasma turbulent transport. Besides, the NFR explicitly depends on only $\mathcal{T}$ and $\mathcal{Z}$, but not on the detailed plasma and equilibrium parameters. This property is useful for estimating turbulent transport with reduced computational costs. Moreover, the NFR approach encourages new capabilities to suggest the optimal quantities and functional forms be learned in deep neural network modelings. The NFR itself can not reduce the computational costs in the transport simulations, because $\mathcal{T}$ and $\mathcal{Z}$ are obtained from nonlinear simulation. There are several works on constructing further simplified transport modeling by utilizing the NFR [18–22]. It also can be applicable to construct global flux driven turbulent simulations such as GT5D [27], GKNET [41], and GYSELA [42]. As shown in figure 3, we can see that the turbulent spectrum shape is rather different for near- and far-marginal cases. Such spectral shape in the wavenumber space is needed to incorporate in future work. Also, the predator-prey like low-frequency oscillation [43] may occur in the collisional plasma. However, the present NFR has not treated such dynamics. Also, the frequency decomposition is not applied to $\mathcal{Z}$ and $\mathcal{T}$ so that the contribution for high-frequency GAM oscillation [44] in $\mathcal{Z}$ is not distinguished. Such additional flexibility may be useful to improve the physical reproductivity. Also, extending NFR to multiple particle species is an important issue. These issues remain to be addressed in future work and will be reported elsewhere.

Data availability statement

All data that support the findings of this study are included within the article (and any supplementary files).

Acknowledgments

The authors would like to thank Dr E Narita, Dr M Yoshida, and Mr K Fujii for useful discussions on this study. This work is supported by JST SPRING, Grant No. JPMJSP2104, in part by the MEXT Japan, Grant Nos. 20K03907, and 17K07001, in part by the NIFS collaborative Research Programs (NIFS21KNST191, NIFS17KNST115, NIFS22KIST017, NIFS22KIST018), and in part by JST, PRESTO Grant Number JPMJPR21O7, Japan, and in part by PLADyS, JSPS Core-to-Core Program. Numerical simulations were performed by JFRS-1 at IFERC- CSC, and Plasma Simulator at NIFS.

ORCID iDs

Nakayama T https://orcid.org/0000-0002-6719-9013
M Nakata https://orcid.org/0000-0003-2693-4859
M Honda https://orcid.org/0000-0003-3942-0080
M Nunami https://orcid.org/0000-0002-2459-2392
S Matsuoka https://orcid.org/0000-0003-2790-2226

References

[1] Idomura Y 2014 Full-*f* gyrokinetic simulation over a confinement time *Phys. Plasmas* **21** 022517
[2] Merlo G, Dominski J, Bhattacharjee A, Chang C S, Jenko F, Ku S, Lanti E and Parker S 2018 Cross-verification of the global gyrokinetic codes GENE and XGC *Phys. Plasmas* **25** 062308
[3] TASK (available at: https://bpsi.nucleng.kyoto-u.ac.jp/task/)
[4] Honda M and Fukuyama A 2008 Dynamic transport simulation code including plasma rotation and radial electric field *J. Comput. Phys.* **227** 2808–44
[5] Yokoyama M, Wakasa A, Seki R, Sato M, Murakami S, Suzuki C, Nakamura Y and Fukuyama A (LHD Experiment Group) 2012 Development of integrated transport code, TASK3D and its applications to LHD experiment *Plasma Fusion Res.* **7** 2403011
[6] Hayashi N and JT-60 Team 2010 Advanced tokamak research with integrated modeling in JT-60 upgrade *Phys. Plasmas* **17** 056112
[7] Honda M, Satake S, Suzuki Y, Matsunaga G, Shinohara K, Yoshida M, Matsuyama A, Ide S and Urano H 2014 Experimental analyses and predictive simulations of toroidal rotation driven by the neoclassical toroidal viscosity in rippled tokamaks *Nucl. Fusion* **54** 114005
[8] Honda M, Aiba N, Seto H, Narita E and Hayashi N 2021 Development of a novel integrated model GOTRESS+ for predictions and assessment of JT-60SA operation scenarios including the pedestal *Nucl. Fusion* **61** 116029
[9] Honda M and Narita E 2019 Machine-learning assisted steady-state profile predictions using global optimization techniques *Phys. Plasmas* **26** 102307
[10] Honda M and Narita E 2021 Development of a surrogate turbulent transport model and its usefulness in transport simulations *Plasma Fusion Res.* **16** 2403002
[11] Waltz R E, Staebler G M, Dorland W, Hammett G W, Kotschenreuther M and Konings J A 1997 A gyro-Landau-fluid transport model *Phys. Plasmas* **4** 2482
[12] Staebler G M, Kinsey J E and Waltz R E 2005 Gyro-Landau fluid equations for trapped and passing particles *Phys. Plasmas* **12** 102508
[13] Staebler G M, Kinsey J E and Waltz R E 2007 A theory-based transport model with comprehensive physics *Phys. Plasmas* **14** 055909
[14] Kinsey J E, Staebler G M and Waltz R E 2008 The first transport code simulations using the trapped gyro-Landau-fluid model *Phys. Plasmas* **15** 055908
[15] Bourdelle C, Garbet X, Imbeaux F, Casati A, Dubuit N, Guirlet R and Parisot T 2007 A new gyrokinetic quasilinear transport model applied to particle transport in tokamak plasmas *Phys. Plasmas* **14** 112501
[16] Staebler G M, Howard N T, Candy J and Holland C 2017 A model of the saturation of coupled electron and ion scale gyrokinetic turbulence *Nucl. Fusion* **57** 066046
[17] Staebler G M, Waltz R E, Candy J and Kinsey J E 2013 New paradigm for suppression of gyrokinetic turbulence by velocity shear *Phys. Rev. Lett.* **110** 055003
[18] Nunami M, Watanabe T-H and Sugama H 2013 A reduced model for ion temperature gradient turbulent transport in helical plasmas *Phys. Plasmas* **20** 092307
[19] Toda S, Nakata M, Nunami M, Ishizawa A, Watanabe T-H and Sugama H 2017 A reduced transport model for ion heat diffusivity by gyro-kinetic analysis with kinetic electrons in helical plasmas *Plasma Fusion Res.* **12** 1303035
[20] Toda S, Nakata M, Nunami M, Ishizawa A, Watanabe T-H and Sugama H 2019 Modeling of turbulent particle and heat transport in helical plasmas based on gyrokinetic analysis *Phys. Plasmas* **26** 012510
[21] Toda S, Nakata M, Nunami M, Ishizawa A, Watanabe T-H and Sugama H 2019 Transport simulation for helical plasmas by use of gyrokinetic transport model *Plasma Fusion Res.* **14** 3403061–3403061
[22] Toda S, Nunami M and Sugama H 2020 Reduced models of turbulent transport in helical plasmas including effects of zonal flows and trapped electrons *J. Plasma Phys.* **86** 815860304
[23] Citrin J, Breton S, Felici F, Imbeaux F, Aniel T, Artaud J F, Baiocchi B, Bourdelle C, Camenen Y and Garcia J 2015 Real-time capable first principle based modelling of tokamak turbulent transport *Nucl. Fusion* **55** 092001
[24] Meneghini O *et al* 2017 Self-consistent core-pedestal transport simulations with neural network accelerated models *Nucl. Fusion* **57** 086034
[25] Narita E, Honda M, Nakata M, Yoshida M, Takenaga H and Hayashi N 2018 Gyrokinetic modelling of the quasilinear particle flux for plasmas with neutral-beam fuelling *Plasma Phys. Control. Fusion* **60** 025027
[26] Narita E, Honda M, Nakata M, Yoshida M, Hayashi N and Takenaga H 2019 Neural-network-based semi-empirical turbulent particle transport modelling founded on gyrokinetic analyses of JT-60U plasmas *Nucl. Fusion* **59** 106018
[27] Nakata M and Idomura Y 2013 Plasma size and collisionality scaling of ion-temperature-gradient-driven turbulence *Nucl. Fusion* **53** 113039
[28] Dimits A M *et al* 2000 Comparisons and physics basis of tokamak transport models and turbulence simulations *Phys. Plasmas* **7** 969–83
[29] Schekochihin A A, Highcock E G and Cowley S C 2012 Subcritical fluctuations and suppression of turbulence in differentially rotating gyrokinetic plasmas *Plasma Phys. Control. Fusion* **54** 055011
[30] Van Wyk F, Highcock E G, Schekochihin A A, Roach C M, Field A R and Dorland W 2016 Transition to subcritical

turbulence in a tokamak plasma *J. Plasma Phys.* **82** 905820609
[31] Nakata M, Nunami M, Sugama H and Watanabe T-H 2016 Impact of hydrogen isotope species on microinstabilities in helical plasmas *Plasma Phys. Control. Fusion* **58** 074008
[32] Nakata M, Nunami M, Sugama H and Watanabe T-H 2017 Isotope effects on trapped-electron-mode driven turbulence and zonal flows in helical and tokamak plasmas *Phys. Rev. Lett.* **118** 165002
[33] Watanabe T-H and Sugama H 2006 Velocity-space structures of distribution function in toroidal ion temperature gradient turbulence *Nucl. Fusion* **46** 24
[34] Nakata M, Watanabe T-H and Sugama H 2012 Nonlinear entropy transfer via zonal flows in gyrokinetic plasma turbulence *Phys. Plasmas* **19** 022303
[35] Nakata M, Honda M, Yoshida M, Urano H, Nunami M, Maeyama S, Watanabe T-H and Sugama H 2016 Validation studies of gyrokinetic ITG and TEM turbulence simulations in a JT-60U tokamak using multiple flux matching *Nucl. Fusion* **56** 086010
[36] Rosenbluth M N and Hinton F L 1998 Poloidal flow driven by ion-temperature-gradient turbulence in tokamaks *Phys. Rev. Lett.* **80** 724
[37] Diamond P H, Itoh S-I, Itoh K and Hahm T S 2005 Zonal flows in plasma—a review *Plasma Phys. Control. Fusion* **47** R35
[38] Hahm T S, Wang L, Wang W X, Yoon E S and Duthoit F X 2013 Isotopic dependence of residual zonal flows *Nucl. Fusion* **53** 072002
[39] Levenberg K 1944 A method for the solution of certain non-linear problems in least squares *Q. Appl. Math.* **2** 164–8
[40] Marquardt D W 1963 An algorithm for least-squares estimation of nonlinear parameters *J. Soc. Ind. Appl. Math.* **11** 431–41
[41] Wang W, Kishimoto Y, Imadera K, Li J Q and Wang Z X 2018 A mechanism for the formation and sustainment of the self-organized global profile and $E \times B$ staircase in tokamak plasmas *Nucl. Fusion* **58** 056005
[42] Dif-Pradalier G, Hornung G, Garbet X, Ghendrih P, Grandgirard V, Latu G and Sarazin Y 2017 The $E \times B$ staircase of magnetised plasmas *Nucl. Fusion* **57** 066026
[43] Lin Z, Hahm T S, Lee W W, Tang W M and Diamond P H 1999 Effects of collisional zonal flow damping on turbulent transport *Phys. Rev. Lett.* **83** 3645–8
[44] Hahm T S, Beer M A, Lin Z, Hammett G W, Lee W W and Tang W M 1999 Shearing rate of time-dependent $E \times B$ flow *Phys. Plasmas* **6** 922–6
[45] Murakami S *et al* 2015 Integrated transport simulations of high ion temperature plasmas of LHD *Plasma Phys. Control. Fusion* **57** 054009